# Modeling the inelastic deformation and fracture of polymer composites – Part I: Plasticity model

M. Vogler [a], R. Rolfes [a], P.P. Camanho [b],*

[a] Institute of Structural Analysis, Leibniz Universität Hannover, Germany
[b] DEMec, Faculdade de Engenharia, Universidade do Porto, Rua Dr. Roberto Frias, 4200-465 Porto, Portugal

## ARTICLE INFO

## ABSTRACT

A new transversely-isotropic elastic–plastic constitutive model for unidirectional fiber reinforced polymers (FRP) is presented. The model is able to represent the fully nonlinear mechanical behavior under multi-axial loading conditions and under triaxial stress states prior to the onset of cracking. Since associated flow rules often give a wrong prediction of plastic Poisson coefficients, a non-associated flow rule is introduced to provide realistic predictions of the volumetric plastic strains. This paper focusses on the simulation of triaxiality dependent plasticity based nonlinearities of FRP until failure occurs. The onset and propagation of failure is predicted by a new smeared crack model presented in an accompanying paper (Camanho et al., 2012). In order to demonstrate the capabilities of the new material model, a yield surface parameter identification for IM7-8552 carbon epoxy is presented and simulations of quasi-static transverse and off-axis compression tests and of uniaxial compression tests superimposed with various values of hydrostatic pressure are shown as a model verification.

## 1. Introduction

The effective use of polymer composite materials reinforced by unidirectional fibers in aerospace and automotive structures relies on the ability to predict the ultimate load and residual strength of these structures. However, accurate failure predictions are only possible if the stress states for general loading conditions, boundary conditions and load histories are properly defined. Therefore, an accurate representation of the constitutive response of the composite material under multiaxial loading conditions, including high hydrostatic pressures, is required (Rolfes et al., 2008; Vogler et al., 2010). The pre-failure nonlinearities due to yielding of the epoxy resin lead to a redistribution of stresses in a laminate and affect the onset of the ply failure mechanisms (matrix cracking, fiber–matrix pullout, fiber failure). For example, Chang and Chang (1987) demonstrated that the simulation of shear non-linearities is required to accurately predict the failure of composite bolted joints manufactured using cross-ply laminates. However, also other nonlinearities must be taken into account (Pinho et al., 2006; Maimi et al., 2011). Especially the pronounced nonlinearities under uniaxial and biaxial compression transverse to the fibers, and under high hydrostatic pressures has to be regarded. In the presence of high pressures the glass transition temperature of the epoxy resin drops from above 80° to operating temperature, which results in a change of the mechanical properties of the lamina (Pae and Rhee, 1995); the elastic parameters are reduced and the epoxy resin exhibits pronounced yielding under high pressure (Mi and Zheng, 1998; Dupaix and Boyce, 2007). Constitutive models, which are able to capture all these non-linearities under multiaxial loading conditions and triaxial stress states does not exist. Furthermore, most of the available models are only valid for the plane stress state (Sun and Chen, 1989). However, general models that simulate plastic deformation and fracture of polymer composites under fully three-dimensional stress states are required.

---

\* Corresponding author.
  E-mail address: pcamanho@fe.up.pt (P.P. Camanho).

Based on the previous observations, the objective of this paper is to present a fully three-dimensional transversely-isotropic elastic–plastic constitutive model for composite materials, which is able to regard all the plasticity based non-linearities under multiaxial loading conditions. The plasticity model proposed here is used in combination with a smeared crack model, presented in an accompanying paper (Camanho et al., 2012), that is able to simulate the onset and propagation of ply failure mechanisms. The plasticity model provides the stress and strain tensors that are used in appropriate failure criteria that distinguish matrix-dominated and fiber-dominated failure mechanisms and that predict the fracture angle; all this information is required for the smeared crack model.

## 2. Transversely isotropic elastic–plastic constitutive model

The material model proposed in this series of two papers consists of an elastic–plastic constitutive model and a smeared crack model. For the overall model, an additive split of the strain tensor into elastic strains $\boldsymbol{\varepsilon}^e$, plastic strains $\boldsymbol{\varepsilon}^p$ and cracking strains $\boldsymbol{\varepsilon}^c$ is assumed:

$$\boldsymbol{\varepsilon} = \boldsymbol{\varepsilon}^e + \boldsymbol{\varepsilon}^p + \boldsymbol{\varepsilon}^c. \tag{1}$$

The material behavior prior to the onset of cracking is governed by the elastic–plastic stress–strain relations, addressed in this paper. The onset and propagation of failure following a traction separation approach for the cracking strains $\boldsymbol{\varepsilon}^c$ is governed by the smeared crack model, presented in Camanho et al. (2012). A scheme of the combined plasticity and smeared crack model is shown in Fig. 1. To establish the constitutive equations for the transversely elastic–plastic material model, the mathematical framework of invariant theory is used. This mathematical concept enables the representation of anisotropic constitutive functions as isotropic tensor functions. An in-deep description of the invariant theory is given in Boehler (1987) and Spencer (1987). A detailed description of the invariant theory with respect to the construction of anisotropic yield functions and anisotropic constitutive equations in general is given in Schröder (1995).

Transversely isotropic materials are characterized by a preferred direction $\mathbf{a}$, which is the fiber direction for unidirectional fiber composites. Thus, the material response is invariant with respect to arbitrary rotations around this preferred direction $\mathbf{a}$, to reflections at fiber parallel planes, and with respect to the reflection at that plane, whose
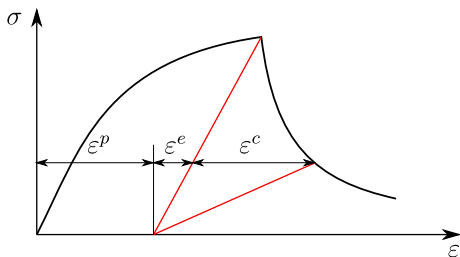


**Fig. 1.** Schematic representation of uniaxial stress–strain response.

normal is $\mathbf{a}$. These are the group of symmetry transformations for transverse isotropy. The structural tensor $\mathbf{A}$ of transverse isotropy, which represents the material's intrinsic characteristic direction, is defined as the dyadic product of the preferred direction $\mathbf{a}$:

$$\mathbf{A} = \mathbf{a} \otimes \mathbf{a}. \tag{2}$$

The structural tensor $\mathbf{A}$ is used as an additional tensor argument to formulate the elastic free energy density, the yield function and the plastic potential as isotropic tensor functions.

### 2.1. Elastic stress strain relations

A linear elastic constitutive law is chosen to describe the elastic stress strain relations. The elastic free energy density for a transversely-isotropic material with the tensorial arguments $\boldsymbol{\varepsilon}$ and $\mathbf{A}$ reads:

$$\hat{\Psi}(\boldsymbol{\varepsilon}, \mathbf{A}) := \frac{1}{2}\lambda(\operatorname{tr}\boldsymbol{\varepsilon})^2 + \mu_T \operatorname{tr}(\boldsymbol{\varepsilon})^2 + \alpha(\mathbf{a}\boldsymbol{\varepsilon}\mathbf{a})\operatorname{tr}\boldsymbol{\varepsilon}$$
$$+ 2(\mu_L - \mu_T)(\mathbf{a}\boldsymbol{\varepsilon}^2\mathbf{a}) + \frac{1}{2}\beta(\mathbf{a}\boldsymbol{\varepsilon}\mathbf{a})^2, \tag{3}$$

with the five elasticity constants $\lambda$, $\alpha$, $\mu_L$, $\mu_T$ and $\beta$ as invariant coefficients. The stresses are obtained by the first derivative of the elastic free energy density with respect to the strains:

$$\boldsymbol{\sigma} = \partial_{\boldsymbol{\varepsilon}}\hat{\Psi}(\boldsymbol{\varepsilon}, \mathbf{A}) = \lambda(\operatorname{tr}\boldsymbol{\varepsilon})\mathbf{1} + 2\mu_T\boldsymbol{\varepsilon} + \alpha(\mathbf{a}\boldsymbol{\varepsilon}\mathbf{a}\mathbf{1} + \operatorname{tr}\boldsymbol{\varepsilon}\mathbf{A})$$
$$+ 2(\mu_L - \mu_T)(\mathbf{A}\boldsymbol{\varepsilon} + \boldsymbol{\varepsilon}\mathbf{A}) + \beta(\mathbf{a}\boldsymbol{\varepsilon}\mathbf{a})\mathbf{A} \tag{4}$$

and the elasticity tensor is given by the second derivative of the elastic free energy density with respect to the strain tensor:

$$\mathbb{C}_e = \partial^2_{\boldsymbol{\varepsilon}\boldsymbol{\varepsilon}}\hat{\Psi}(\boldsymbol{\varepsilon}, \mathbf{A}) = \lambda\mathbf{1}\otimes\mathbf{1} + 2\mu_T\mathbb{I} + \alpha(\mathbf{A}\otimes\mathbf{1} + \mathbf{1}\otimes\mathbf{A})$$
$$+ 2(\mu_L - \mu_T)\mathbb{I}_{\mathbf{A}} + \beta\mathbf{A}\otimes\mathbf{A}, \tag{5}$$

with

$$\mathbb{I}_{\mathbf{A}} = A_{im}\mathbb{I}_{jmkl} + A_{jm}\mathbb{I}_{mikl}. \tag{6}$$

In matrix notation, the 4th order elasticity tensor of a transversely-isotropic material for the preferred $X_1$-direction in a Cartesian coordinate system, i.e. $\mathbf{a} = [1, 0, 0]^T$, reads:

$$\mathbb{C}_e = \begin{bmatrix} \lambda+2\alpha+\beta+4\mu_L-2\mu_T & \lambda+\alpha & \lambda+\alpha & 0 & 0 & 0 \\ \lambda+\alpha & \lambda+2\mu_T & \lambda & 0 & 0 & 0 \\ \lambda+\alpha & \lambda & \lambda+2\mu_T & 0 & 0 & 0 \\ 0 & 0 & 0 & \mu_L & 0 & 0 \\ 0 & 0 & 0 & 0 & \mu_L & 0 \\ 0 & 0 & 0 & 0 & 0 & \mu_T \end{bmatrix}. \tag{7}$$

A conversion from invariant coefficients to engineering coefficients and vice versa is given in Table 3, see Appendix.

### 2.2. Yield function and definition of invariants

The structural tensor $\mathbf{A}$ and the stress tensor $\boldsymbol{\sigma}$ are the argument tensors, whose isotropic invariants form the functional basis for constructing the yield function $f$ as a

scalar isotropic tensor function. Since an isotropic hardening rule is applied, the equivalent plastic strain $\bar{\varepsilon}^p$ defined in Eq. (22) is needed as an additional argument of the yield function. The general form of the yield function reads

$$f = f(\boldsymbol{\sigma}, \bar{\varepsilon}^p, \mathbf{A}) \leqslant 0. \tag{8}$$

The functional basis for transverse isotropy formed by the argument tensors $\mathbf{A}$ and $\boldsymbol{\sigma}$ reads

$$\mathrm{tr}[\boldsymbol{\sigma}], \quad \mathrm{tr}[\boldsymbol{\sigma}^2], \quad \mathrm{tr}[\boldsymbol{\sigma}^3], \quad \mathrm{tr}[\mathbf{A}\boldsymbol{\sigma}] \quad \text{and} \quad \mathrm{tr}[\mathbf{A}\boldsymbol{\sigma}^2]. \tag{9}$$

In accordance with the invariant theory, an arbitrary linear combination of the stress tensor $\boldsymbol{\sigma}$ can be used in Eq. (9). Furthermore, a linear combination of the basic invariants given in (9) can be used without loss of generality. Hereafter, the quadratic invariants $\mathrm{tr}[\boldsymbol{\sigma}^2]$ and $\mathrm{tr}[\mathbf{A}\boldsymbol{\sigma}^2]$ and the linear invariant $\mathrm{tr}[\boldsymbol{\sigma}]$ of the functional basis (9) are reformulated in order to identify certain stress states with the corresponding invariants. The basic invariants $\mathrm{tr}[\mathbf{A}\boldsymbol{\sigma}]$ and $\mathrm{tr}[\boldsymbol{\sigma}^3]$ are neglected. The invariant $\mathrm{tr}[\mathbf{A}\boldsymbol{\sigma}]$ can be used to regard yielding in fiber direction, as it occurs in short fiber reinforced thermoplastics, the cubic invariant $\mathrm{tr}[\boldsymbol{\sigma}^3]$ is suitable for modeling metal plasticity. For reformulating the quadratic invariants of the functional basis (9), i.e. $\mathrm{tr}[\boldsymbol{\sigma}^2]$ and $\mathrm{tr}[\mathbf{A}\boldsymbol{\sigma}^2]$, a decomposition of the stress tensor $\boldsymbol{\sigma}$ in plasticity inducing stresses $\boldsymbol{\sigma}^{\mathrm{pind}}$ and reaction stresses $\boldsymbol{\sigma}^{\mathrm{reac}}$ is assumed (Spencer, 1972; Rogers, 1987; Schröder, 1995):

$$\boldsymbol{\sigma} = \boldsymbol{\sigma}^{\mathrm{pind}} + \boldsymbol{\sigma}^{\mathrm{reac}}, \tag{10}$$

with the stress components $\boldsymbol{\sigma}^{\mathrm{reac}}$ and $\boldsymbol{\sigma}^{\mathrm{pind}}$ :

$$\begin{aligned} \boldsymbol{\sigma}^{\mathrm{reac}} &= \frac{1}{2}(\mathrm{tr}\,\boldsymbol{\sigma} - \mathbf{a}\boldsymbol{\sigma}\mathbf{a})\mathbf{1} - \frac{1}{2}(\mathrm{tr}\,\boldsymbol{\sigma} - 3\mathbf{a}\boldsymbol{\sigma}\mathbf{a})\mathbf{A}, \\ \boldsymbol{\sigma}^{\mathrm{pind}} &= \boldsymbol{\sigma} - \frac{1}{2}(\mathrm{tr}\,\boldsymbol{\sigma} - \mathbf{a}\boldsymbol{\sigma}\mathbf{a})\mathbf{1} + \frac{1}{2}(\mathrm{tr}\,\boldsymbol{\sigma} - 3\mathbf{a}\boldsymbol{\sigma}\mathbf{a})\mathbf{A}. \end{aligned} \tag{11}$$

The stress tensor $\boldsymbol{\sigma}^{\mathrm{reac}}$ is called the reaction stress tensor, because it contains the hydrostatic pressure and the projection of the stress tensor onto the preferred direction $\mathbf{a}$. The hydrostatic pressure and the stresses in fiber direction are at first assumed to result in elastic reactions. Reformulation of the quadratic invariants using $\boldsymbol{\sigma}^{\mathrm{pind}}$ gives the invariants $I_1$ and $I_2$, see Eq. (12). The choice of the plasticity inducing stresses $\boldsymbol{\sigma}^{\mathrm{pind}}$ instead of $\boldsymbol{\sigma}$ for reformulating the quadratic invariants of the functional basis enables to identify transverse shear loading solely with the invariant $I_1$ and in-plane shear loading solely with the invariant $I_2$. Hence, a complete decoupling of the stress states with respect to their representation by invariants is achieved. This significantly simplifies the parameter identification. In order to account for pressure dependent yielding, the linear invariant $\mathrm{tr}[\boldsymbol{\sigma}]$ of the functional basis (9) is reformulated, which gives the third invariant $I_3$ in Eq. (12). The set of transversely isotropic invariants used to formulate the yield surface reads:

$$\begin{aligned} I_1 &:= \frac{1}{2}\,\mathrm{tr}\left(\boldsymbol{\sigma}^{\mathrm{pind}}\right)^2 - \mathbf{a}\left(\boldsymbol{\sigma}^{\mathrm{pind}}\right)^2\mathbf{a}, \\ I_2 &:= \mathbf{a}\left(\boldsymbol{\sigma}^{\mathrm{pind}}\right)^2\mathbf{a}, \\ I_3 &:= \mathrm{tr}\,\boldsymbol{\sigma} - \mathbf{a}\boldsymbol{\sigma}\mathbf{a}. \end{aligned} \tag{12}$$

Having defined the set of invariants (12), the transversely isotropic yield surface formulation for unidirectional fiber matrix composites is introduced:

$$f(\boldsymbol{\sigma}, \bar{\varepsilon}^p, \mathbf{A}) = \alpha_1 I_1 + \alpha_2 I_2 + \alpha_3 I_3 + \alpha_{32} I_3^2 - 1 \leqslant 0, \tag{13}$$

with

$$\begin{aligned} \alpha_3 &= \alpha_3^t, \quad \alpha_{32} = \alpha_{32}^t \quad \text{if } I_3 > 0 \quad \text{and} \\ \alpha_3 &= \alpha_3^c, \quad \alpha_{32} = \alpha_{32}^c \quad \text{if } I_3 \leqslant 0. \end{aligned} \tag{14}$$

As an extension of the yield surface presented in Vogler et al. (2010), the case differentiation concerning $I_3$ into $I_3 > 0$ and $I_3 < 0$ allows additionally to control yielding in biaxial stress states. Especially the consideration of the biaxial compression hardening behavior is crucial for modeling the response of carbon epoxy under high hydrostatic pressures. The proposed yield function results in six yield surface parameters that have to be determined. Each one of these parameters and the corresponding invariants are related to certain loading states: transverse shear, in-plane shear, uniaxial and biaxial tension and uniaxial and biaxial compression. For each of these loading states, a hardening curve can be prescribed, giving yield stress vs. corresponding plastic strain. The implemented isotropic hardening rule ensures, that the hardening curves prescribed in each stress state are recovered exactly in the simulations. It is understood, that the material behavior exhibits both isotropic and kinematic hardening and that a proper constitutive model should regard a combination of both. However, in order to get information about the percentage of kinematic hardening, unloading tests with subsequent load reversal has to be performed. For convenience and due to a lack of experimental data an isotropic hardening rule is used. The determination of the yield surface parameters based on the prescribed hardening curves in each stress state is described in detail in Section 2.4.

Illustrations of the yield surface can be generated in stress space or in invariant space, defined by the transversely isotropic invariants summarized in Eq. (12). Having defined a set of yield surface parameters, the representation in invariant space is unique. Furthermore, it is independent from the coordinate system selected. In contrast, representations in stress space are not unique, since each point in the invariant space has various representations in stress space. Hence, the representation of the yield surface in the invariant space is more general. Fig. 2 shows a schematic representation of the yield surface in the $\sigma_{22}$–$\sigma_{33}$ stress space and in the $\sigma_{22}$–$\tau_{12}$ stress space. A representation of the transversely isotropic yield surface in invariant space is shown in Fig. 3. On the left-hand side, a representation in $I_3$–$\sqrt{I_1}$-space is shown, setting $I_2 = 0$. The interaction between yielding under transverse shear, under uniaxial and under biaxial loadings can be seen. The right-hand side in Fig. 3 gives a representation of the yield locus in $\sqrt{I_1}$–$\sqrt{I_2}$-plane ($I_3 = 0$), showing the interaction between transverse and in-plane shear. In both illustrations, the highlighted points are the "trigger points" of the yield surface, in which yielding is controlled. That is, in each of these points, an initial yield stress and a hardening curve, giving the yield stress over the corresponding plastic strain, can be predetermined. This is explained in detail in Section 2.4.

For the algorithmic treatment within the framework of a finite element analysis, the first and second derivatives of
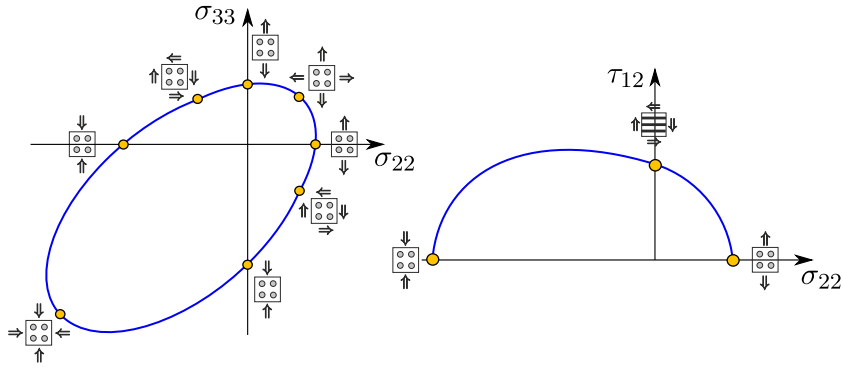
**Fig. 2.** Schematic representation of the yield surface in stress space.
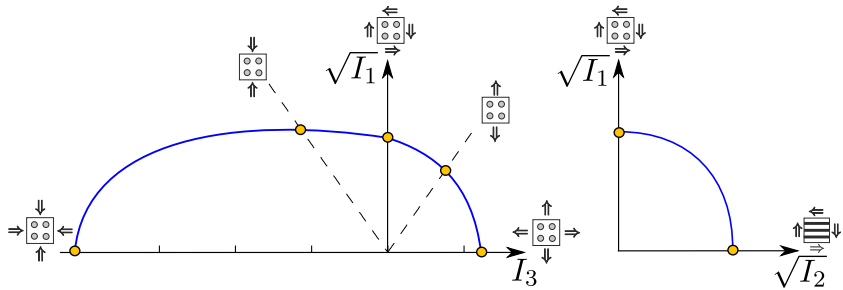


**Fig. 3.** Schematic representation of the yield surface in invariant space.

the yield surface given in Eq. (13) with respect to the stresses are required:

$$\mathbf{n}_f := \partial_{\boldsymbol{\sigma}} f = \partial_{I_i} f \, \partial_{\boldsymbol{\sigma}} I_i = \alpha_1 \boldsymbol{\sigma}^{\text{pind}} + (\alpha_2 - \alpha_1)(\mathbf{A}\boldsymbol{\sigma}^{\text{pind}} + \boldsymbol{\sigma}^{\text{pind}}\mathbf{A})$$
$$+ \alpha_3(\mathbf{1} - \mathbf{A}) + 2\alpha_{32} I_3(\mathbf{1} - \mathbf{A}) + =: \mathbb{K} : \boldsymbol{\sigma} + \mathbf{L}$$

$$\partial_{\boldsymbol{\sigma}\boldsymbol{\sigma}}^2 f = \alpha_1 \, \mathbb{P}^{\text{pind}} + (\alpha_2 - \alpha_1) \, \mathbb{P}_{\mathbf{A}}^{\text{pind}} + 2\alpha_{32}(\mathbf{1} - \mathbf{A}) \otimes (\mathbf{1} - \mathbf{A})$$
$$=: \mathbb{K} \tag{15}$$

with the projection tensors defined as:

$$\mathbb{P}^{pind} := \partial_{\boldsymbol{\sigma}} \boldsymbol{\sigma}^{\text{pind}} = \mathbb{I} - \frac{1}{2}(\mathbf{1} \otimes \mathbf{1}) + \frac{1}{2}(\mathbf{A} \otimes \mathbf{1} + \mathbf{1} \otimes \mathbf{A}) - \frac{3}{2}(\mathbf{A} \otimes \mathbf{A}) \text{ and}$$
$$\mathbb{P}_{\mathbf{A}}^{pind} = P_{\mathbf{A}\,ijkl}^{\text{pind}} := A_{im} P_{mjkl}^{\text{pind}} + A_{mj} P_{imkl}^{\text{pind}}. \tag{16}$$

$\mathbb{K}$ is the constant bending tensor and $\mathbf{L}$ is the first derivative of the linear terms in $\boldsymbol{\sigma}$ of the yield surface formulation. With the derivatives Eq. (15), the yield function Eq. (13) reads in a more general form:

$$f(\boldsymbol{\sigma}, \bar{\varepsilon}^p, \mathbf{A}) = \frac{1}{2}\boldsymbol{\sigma} : \mathbb{K} : \boldsymbol{\sigma} + \mathbf{L} : \boldsymbol{\sigma} - 1 \leqslant 0. \tag{17}$$

### 2.3. Plastic potential

As an extension of the model presented in Vogler et al., 2010, a non-associated flow rule is introduced in this paper. That is, the evolution of the plastic strains is not given by the gradient of the yield surface $\mathbf{n}_f := \partial_{\boldsymbol{\sigma}} f$ (associated flow), but by the gradient of a plastic potential function $\mathbf{n}_g := \partial_{\boldsymbol{\sigma}} g$, where $g = g(\boldsymbol{\sigma}, \mathbf{A})$ is the so called plastic flow potential. The choice of a non-associated flow rule allows

the accurate prediction of the plastic Poisson coefficients and of the volumetric plastic strains. The formulation of the plastic potential $g = g(\boldsymbol{\sigma}, \mathbf{A})$ is similar to the yield function (13); however, the linear term $I_3$ is omitted. The plastic flow potential is defined as

$$g(\boldsymbol{\sigma}, \mathbf{A}) = \beta_1 I_1 + \beta_2 I_2 + \beta_3 I_3^2 - 1. \tag{18}$$

The determination of the plastic potential parameters $\beta_1$, $\beta_2$ and $\beta_3$ with the objective to achieve a certain Poisson coefficient is given in Section 2.4.2. For the time integration of the constitutive equations, the first and second derivative of $g = g(\boldsymbol{\sigma}, \mathbf{A})$ with respect to the stresses are required, see also Eq. (15). The forth order tensor $\mathbb{M}$ reads:

$$\mathbb{M} = \beta_1 \, \mathbb{P}^{pind} + (\beta_2 - \beta_1) \, \mathbb{P}_{\mathbf{A}}^{pind} + 2\beta_{32}(\mathbf{1} - \mathbf{A}) \otimes (\mathbf{1} - \mathbf{A}), \tag{19}$$

where the projection tensors $\mathbb{P}^{pind}$ and $\mathbb{P}_{\mathbf{A}}^{pind}$ are given in Eq. (16). The first derivative of the plastic potential with respect to the stresses reads:

$$\mathbf{n}_g := \partial_{\boldsymbol{\sigma}} g = \mathbb{M} : \boldsymbol{\sigma}. \tag{20}$$

The plastic flow potential Eq. (18) reads in a more general form:

$$g(\boldsymbol{\sigma}, \mathbf{A}) = \frac{1}{2}\boldsymbol{\sigma} : \mathbb{M} : \boldsymbol{\sigma} - 1. \tag{21}$$

### 2.4. Parameter identification

In the following, the determination of the six yield surface parameters in Eq. (13) and of the three plastic potential parameters in Eq. (18) is explained in detail.

### 2.4.1. Yield surface parameters

For each of the trigger points of the yield locus, the initial yield stress and a hardening curve, giving yield stress vs. corresponding plastic strain, can be determined. The corresponding plastic strain in each loading state is related to the equivalent plastic strain, which is defined here as

$$\bar{\varepsilon}^p := \sqrt{\frac{1}{2}}\|\boldsymbol{\varepsilon}^p\| = \sqrt{\frac{1}{2}\varepsilon_{ij}^p\varepsilon_{ij}^p}. \tag{22}$$

Note that this is not the equivalent plastic strain used in von Mises plasticity. The plastic strains in uniaxial loading transverse, biaxial loading transverse and shear loading (in-plane and transverse) are related by a corresponding factor with the equivalent plastic strain $\bar{\varepsilon}^p$ :
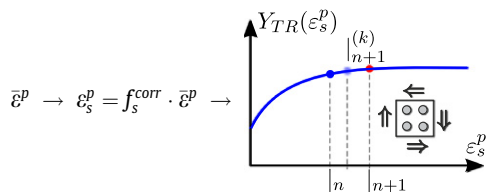
$$\begin{aligned}
\varepsilon_{uni}^p &= f_{uni}^{corr} \cdot \bar{\varepsilon}^p \\
\varepsilon_{bi}^p &= f_{bi}^{corr} \cdot \bar{\varepsilon}^p \\
\varepsilon_s^p &= f_s^{corr} \cdot \bar{\varepsilon}^p
\end{aligned} \tag{23}$$

The factors $f_{uni}^{corr}$, $f_{bi}^{corr}$ and $f_s^{corr}$ in Eq. (23) are directly dependent on the choice of the plastic potential parameters $\beta_1$, $\beta_2$ and $\beta_3$ in Eq. (18). The determination of these factors is explained in Section 2.4.2.

For each loading state, a hardening curve giving yield stress $Y_{(..)}$ vs. corresponding plastic strain $\varepsilon_{(..)}^p$ must be prescribed for transverse shear $Y_{TR}(\varepsilon_s^p)$, in-plane shear $Y_{IP}(\varepsilon_s^p)$, uniaxial tension $Y_{UT}(\varepsilon_{uni}^p)$, biaxial tension $Y_{BT}(\varepsilon_{bi}^p)$, uniaxial compression $Y_{UC}(\varepsilon_{uni}^p)$ and biaxial compression $Y_{BC}(\varepsilon_{bi}^p)$. These hardening curves are directly recovered in the plasticity model by use of an isotropic hardening formulation. In the algorithmic treatment required for the finite element analysis, the hardening curves are given as tabulated data. In each time step, a Table lookup is performed with the equivalent plastic strain $\bar{\varepsilon}^p$ as input value. Using Eq. (23), the plastic strain for each stress state is obtained and the corresponding yield stress is given by the respective hardening curve. Having obtained the current yield stress via Table lookup, an update of the yield surface parameters $\alpha_{(..)}$ is done. Since the yield stresses $Y_{(..)} = Y_{(..)}(\bar{\varepsilon}^p)$ depend on the equivalent plastic strain $\bar{\varepsilon}^p$, the $\alpha_{(..)}$-parameters of the yield surface formulation are also dependent on the equivalent plastic strain, i.e. $\alpha_{(..)} = \alpha_{(..)}(\bar{\varepsilon}^p)$. For reasons of readability, this is omitted in Eqs. (24)–(33).

In the following, the determination of the yield surface parameters $\alpha_{(..)} = \alpha_{(..)}(\bar{\varepsilon}^p)$ is explained in detail. The vector of the preferred direction is set to $a = \begin{bmatrix} 1 & 0 & 0 \end{bmatrix}^T$, i.e. the 1-direction is the fiber direction.

1. Transverse shear



$$\bar{\varepsilon}^p \rightarrow \varepsilon_s^p = f_s^{corr} \cdot \bar{\varepsilon}^p \rightarrow$$
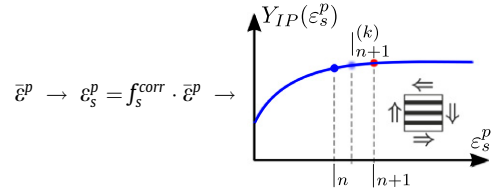
$$\rightarrow Y_{TR}^{(k)} \rightarrow \boldsymbol{\sigma} = \begin{bmatrix} 0 & 0 & 0 \\ 0 & 0 & Y_{TR} \\ 0 & Y_{TR} & 0 \end{bmatrix} \rightarrow I_1 = Y_{TR}^2,$$

$$I_2 = 0, \quad I_3 = 0$$

Inserting the invariants into the yield condition Eq. (13) gives:

$$f = \alpha_1 Y_{TR}^2 - 1 = 0 \rightarrow \boxed{\alpha_1 = 1/Y_{TR}^2} \tag{24}$$

2. In-plane shear



$$\bar{\varepsilon}^p \rightarrow \varepsilon_s^p = f_s^{corr} \cdot \bar{\varepsilon}^p \rightarrow$$
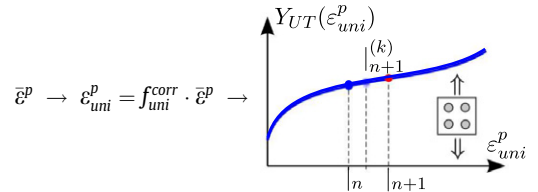
$$\rightarrow Y_{IP}^{(k)} \rightarrow \boldsymbol{\sigma} = \begin{bmatrix} 0 & Y_{IP} & 0 \\ Y_{IP} & 0 & 0 \\ 0 & 0 & 0 \end{bmatrix} \rightarrow I_1 = 0,$$

$$I_2 = Y_{IP}^2, \quad I_3 = 0$$

Inserting the invariants into the yield condition Eq. (13) gives:

$$f = \alpha_2 Y_{IP}^2 - 1 = 0 \rightarrow \boxed{\alpha_2 = 1/Y_{IP}^2} \tag{25}$$

3. Transverse uniaxial tension



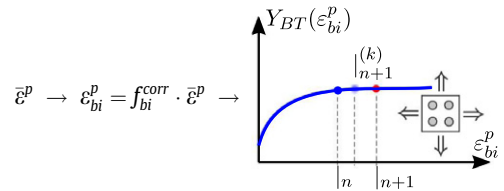$$\bar{\varepsilon}^p \rightarrow \varepsilon_{uni}^p = f_{uni}^{corr} \cdot \bar{\varepsilon}^p \rightarrow$$

$$\rightarrow Y_{UT}^{(k)} \rightarrow \boldsymbol{\sigma} = \begin{bmatrix} 0 & 0 & 0 \\ 0 & Y_{UT} & 0 \\ 0 & 0 & 0 \end{bmatrix} \rightarrow I_1 = \frac{Y_{UT}^2}{4},$$

$$I_2 = 0, \quad I_3 = Y_{UT}$$

Inserting the invariants into the yield condition Eq. (13) gives:

$$f = \alpha_1 \frac{Y_{UT}^2}{4} + \alpha_3^t Y_{UT} + \alpha_{32}^t (Y_{UT})^2 - 1 = 0 \tag{26}$$

4. Transverse biaxial tension



$$\bar{\varepsilon}^p \rightarrow \varepsilon_{bi}^p = f_{bi}^{corr} \cdot \bar{\varepsilon}^p \rightarrow$$

$$\rightarrow Y_T^{(k)} \rightarrow \boldsymbol{\sigma} = \begin{bmatrix} 0 & 0 & 0 \\ 0 & Y_{BT} & 0 \\ 0 & 0 & Y_{BT} \end{bmatrix} \rightarrow I_1 = 0,$$

$$I_2 = 0, \quad I_3 = 2Y_{BT}$$

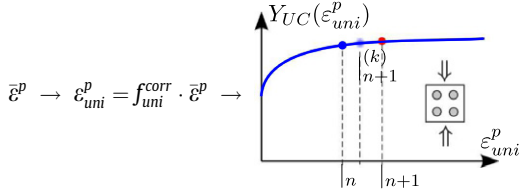Inserting the invariants into the yield condition Eq. (13) gives:

$$f = 2\alpha_3^t Y_{BT} + 4\alpha_{32}^t (Y_{BT})^2 - 1 = 0 \tag{27}$$

Having defined $\alpha_1$ (Eq. (24)), equations (26) and (27) can be solved for $\alpha_3^t$ and $\alpha_{32}^t$:

$$\rightarrow \boxed{\alpha_{32}^t = \frac{1 - \frac{Y_T}{2Y_{BT}} - \alpha_1 \frac{Y_T^2}{4}}{Y_T^2 - 2Y_{BT}Y_T}} \tag{28}$$

$$\rightarrow \boxed{\alpha_3^t = \frac{1}{2Y_{BT}} - 2\alpha_{32}^t Y_{BT}} \tag{29}$$
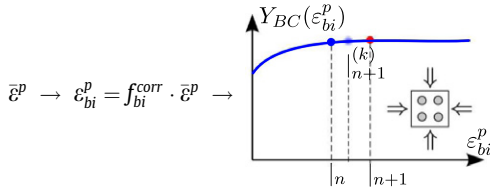
5. Transverse uniaxial compression



$$\bar{\varepsilon}^p \rightarrow \varepsilon_{uni}^p = f_{uni}^{corr} \cdot \bar{\varepsilon}^p \rightarrow$$

$$\rightarrow Y_{UC}^{(k)} \rightarrow \boldsymbol{\sigma} = \begin{bmatrix} 0 & 0 & 0 \\ 0 & Y_{UC} & 0 \\ 0 & 0 & 0 \end{bmatrix} \rightarrow I_1 = \frac{(Y_{UC})^2}{4},$$

$$I_2 = 0, \quad I_3 = -Y_{UC}$$

Inserting the invariants into the yield function Eq. (13) results in:

$$f = \alpha_1 \frac{(Y_{UC})^2}{4} - \alpha_3^c Y_{UC} + \alpha_{32}^c (Y_{UC})^2 - 1 = 0 \tag{30}$$



$$\bar{\varepsilon}^p \rightarrow \varepsilon_{bi}^p = f_{bi}^{corr} \cdot \bar{\varepsilon}^p \rightarrow$$

$$\rightarrow Y_{BC}^{(k)} \rightarrow \boldsymbol{\sigma} = \begin{bmatrix} 0 & 0 & 0 \\ 0 & Y_{BC} & 0 \\ 0 & 0 & Y_{BC} \end{bmatrix}$$

6. Transverse biaxial compression

$$\rightarrow I_1 = 0, \quad I_2 = 0, \quad I_3 = -2Y_{BC}$$

Inserting the invariants into the yield function Eq. (13) yields:

$$f = -2\alpha_3^c Y_{BC} + 4\alpha_{32}^c (Y_{BC})^2 - 1 = 0 \tag{31}$$

Having defined $\alpha_1$ (Eq. (24)), Eqs. (30) and (31) can be solved for $\alpha_3^c$ and $\alpha_{32}^c$:

$$\rightarrow \boxed{\alpha_{32}^c = \frac{1 - \frac{Y_C}{2Y_{BC}} - \alpha_1 \frac{Y_C^2}{4}}{Y_C^2 - 2Y_{BC}Y_C}} \tag{32}$$

$$\rightarrow \boxed{\alpha_3^c = \frac{1}{2Y_{BC}} - 2\alpha_{32}^c Y_{BC}} \tag{33}$$

### 2.4.2. Plastic potential parameters

In order to define the parameters $\beta_1$, $\beta_2$ and $\beta_3$ of the plastic potential function Eq. (18), it is convenient to derive these $\beta_{(.)}$-parameters by stress valued quantities $\hat{Y}_{(.)}$ in the same way as the yield surface parameters $\alpha_{(.)}$ are obtained by the yield stresses $Y_{(.)}$ in various stress states. The $\beta_{(.)}$-values in dependence of the "potential stresses" $\hat{Y}_{(.)}$ read then:

$$\beta_1 = 1/(\hat{Y}_{TR})^2,$$
$$\beta_2 = 1/(\hat{Y}_{IP})^2, \tag{34}$$
$$\beta_3 = \frac{1}{\hat{Y}_U} - \frac{\beta_1}{4},$$

with $\hat{Y}_U = \hat{Y}_{UC} = \hat{Y}_{UT}$. The so called "potential stresses" $\hat{Y}_{(.)}$ have no direct physical meaning. They just serve as parameters in order to construct the plastic potential function in analogy to the yield function. They make physically sense, since they control plastic contractility (dilatancy) during yielding. Furthermore, not the absolute values, but rather the ratios of these values are relevant.

The determination of the potential parameters $\beta_{(.)}$ to obtain a certain plastic Poisson ratio for a uniaxial stress state is demonstrated in the following. The normalized stress tensor for a uniaxial loading in the 2-direction reads

$$\boldsymbol{\sigma}^{uni} = \begin{bmatrix} 0 & 0 & 0 \\ 0 & 1 & 0 \\ 0 & 0 & 0 \end{bmatrix}. \tag{35}$$

Having already defined the plastic potential, the tensor $\mathbb{M}$ is known and the tensor of the plastic strain increments using a non-associated flow rule reads

$$\Delta \boldsymbol{\varepsilon}^{p,uni} = \Delta \gamma_{n+1} \mathbb{M} : \boldsymbol{\sigma}^{uni}, \tag{36}$$

where $\Delta \gamma_{n+1}$ is set to 1, because for defining the contractility and the plastic Poisson coefficients, the ratios of volumetric and deviatoric strains are of interest instead of the absolute values. The plastic Poisson ratio is defined as:

$$\nu_{23}^p := -\frac{\varepsilon_{22}^{p,uni}}{\varepsilon_{33}^{p,uni}} \tag{37}$$

Note that in case of isochoric plastic deformation in the transversely isotropic case, the plastic Poisson coefficient equals 1, since no plastic deformations occur in the fiber direction (1-direction). Compared to the isotropic case, a Poisson ratio $\nu^p = 0.5$ means plastic incompressibility. Since the plastic Poisson ratio is just defined for uniaxial loadings, it does not give any information about contractility and dilatancy in arbitrary stress states. Therefore, the plastic contractility Eq. (39) is introduced as a new quantity. First, the volumetric plastic strain is introduced next:

$$\varepsilon_{vol}^p := \frac{1}{2} \operatorname{tr} \boldsymbol{\varepsilon}^p = \frac{1}{2} \varepsilon_{ii}^p. \tag{38}$$

Note that this is not the definition of the volumetric plastic strain normally used in von Mises plasticity, which reads $\varepsilon_{vol}^p := \frac{1}{3} \operatorname{tr} \boldsymbol{\varepsilon}^p$. Having defined $\varepsilon_{vol}^p$ and with the equivalent plastic strain $\bar{\varepsilon}^p$ Eq. (22), the plastic contractility $\kappa^p$ is introduced:

$$\kappa^p := -\frac{\varepsilon_{vol}^p}{\bar{\varepsilon}^p} \tag{39}$$

In contrast to the plastic Poisson ratio, this quantity can be evaluated in arbitrary stress states giving information about plastic contractility. The plastic contractility $\kappa^p$ has the following properties:

$$-1 \leqslant \kappa^p \leqslant 1,$$

$$\kappa^p < 0 \;\rightarrow\; \text{plastic dilatancy},$$

$$\kappa^p > 0 \;\rightarrow\; \text{plastic compressibility}, \tag{40}$$

$$|\kappa^p| = 1 \;\rightarrow\; \text{all plastic strains are volumetric},$$

$$\kappa^p = 0 \;\rightarrow\; \text{no volumetric plastic strains}.$$

Having determined a set of plastic potential parameters, the factors $f_{uni}^{corr}$, $f_s^{corr}$ and $f_{bi}^{corr}$ used in Eq. (23) have to be calculated:

$$f_{uni}^{corr} := \frac{\varepsilon_{22}^p}{\bar{\varepsilon}^p},$$

$$f_{sh}^{corr} := \frac{\varepsilon_{12}^p}{\bar{\varepsilon}^p}, \tag{41}$$

$$f_{bi}^{corr} := \frac{\varepsilon_{22}^p}{\bar{\varepsilon}^p}.$$

The easiest way to obtain a parameter set predicting a desired plastic Poisson coefficient is to use a simplified optimization procedure. The proposed optimization procedure is summarized in Table 1. It starts with a set of parameters assuming plastic incompressibility. This is the case, when $\hat{Y}_U = 2\hat{Y}_S$ holds. This yields $v^p = -1$, $\varepsilon_{vol}^p = 0$ and $f_{uni}^{corr} = f_s^{corr} = 1$ and the representation of the potential in $I_1$–$I_3$-invariant space (see illustration in Table 1) degenerates to a straight line parallel to the $I_3$-axis. In a next step, the quantity $\hat{Y}_U$ can be reduced stepwise until the desired value for the plastic Poisson ratio is achieved. Note, that in order to have a correct Table lookup of the prescribed plastic hardening curves, the correction factors also change. Therefore, they have to be calculated after the definition of the plastic potential parameters.

### 2.5. Non-associative elastoplasticity

Introducing a non-associated flow rule, the evolution equation for the plastic strains $\boldsymbol{\varepsilon}^p$ reads:

$$\dot{\boldsymbol{\varepsilon}}^p := \gamma \partial_{\boldsymbol{\sigma}} g(\boldsymbol{\sigma}, \mathbf{A}) = \gamma \mathbf{n}_g, \tag{42}$$

with the direction $\mathbf{n}_g$ of the plastic flow defined in Eq. (20). Inserting Eq. (42) into the elasticity law presented in Section 2.1 and using the additive split (1), the stress rate reads:

$$\dot{\boldsymbol{\sigma}} = \mathbb{C}_e : (\dot{\boldsymbol{\varepsilon}} - \dot{\boldsymbol{\varepsilon}}^p) = \mathbb{C}_e : (\dot{\boldsymbol{\varepsilon}} - \gamma \mathbf{n}_g). \tag{43}$$

According to the definition of the equivalent plastic strain Eq. (22), the evolution equation for the equivalent plastic strain $\dot{\bar{\varepsilon}}^p$ reads:

$$\dot{\bar{\varepsilon}}^p := \sqrt{\frac{1}{2}}||\dot{\boldsymbol{\varepsilon}}^p|| = \gamma\sqrt{\frac{1}{2}}||\mathbf{n}_g||. \tag{44}$$

The loading and unloading conditions are given by the Kuhn–Tucker equations:

$$\gamma \geqslant 0; \quad f \leqslant 0; \quad f\gamma = 0. \tag{45}$$

In case of plastic loading $\gamma > 0$ and $f = 0$ holds, for unloading respectively $f < 0$ and $\gamma = 0$. This can be summarized with the consistency condition

$$\dot{f}\gamma = 0. \tag{46}$$

In case of plastic loading $\gamma \neq 0 \wedge \dot{f} = 0$ holds and the consistency parameter $\gamma$ can be obtained from the consistency condition Eq. (46) using $\dot{f} = 0$:

$$\dot{f} = \partial_{\boldsymbol{\sigma}} f \dot{\boldsymbol{\sigma}} + \partial_{\bar{\varepsilon}^p} f \dot{\bar{\varepsilon}}^p \stackrel{!}{=} 0. \tag{47}$$

Inserting (43) and (44) in the consistency condition (47) yields:

$$\dot{f} = \mathbf{n}_f : \mathbb{C}_e : (\dot{\boldsymbol{\varepsilon}} - \gamma\mathbf{n}_g) + (\partial_{\mathbb{K}}f\partial_{\bar{\varepsilon}^p}\mathbb{K} + \partial_{\mathbf{L}}f\partial_{\bar{\varepsilon}^p}\mathbf{L})\sqrt{\frac{1}{2}}||\mathbf{n}_g||\gamma \stackrel{!}{=} 0. \tag{48}$$

The derivatives $\partial_{\bar{\varepsilon}^p}\mathbb{K}$ and $\partial_{\bar{\varepsilon}^p}\mathbf{L}$ are given in Eqs. (67) and (69), see Appendix. Solving Eq. (48) for $\gamma$ yields:

$$\gamma = \frac{\mathbf{n}_f : \mathbb{C}_e : \dot{\boldsymbol{\varepsilon}}}{\mathbf{n}_f : \mathbb{C}_e : \mathbf{n}_g + (\partial_{\mathbb{K}}f\partial_{\bar{\varepsilon}^p}\mathbb{K} + \partial_{\mathbf{L}}f\partial_{\bar{\varepsilon}^p}\mathbf{L})\sqrt{\frac{1}{2}}||\mathbf{n}_g||}. \tag{49}$$

Inserting Eq. (49) into Eq. (43) yields:

$$\dot{\boldsymbol{\sigma}} = \mathbb{C}_e : \left[ \dot{\boldsymbol{\varepsilon}} - \frac{\mathbf{n}_f : \mathbb{C}_e : \dot{\boldsymbol{\varepsilon}}}{\mathbf{n}_f : \mathbb{C}_e : \mathbf{n}_g + (\partial_{\mathbb{K}}f\partial_{\bar{\varepsilon}^p}\mathbb{K} + \partial_{\mathbf{L}}f\partial_{\bar{\varepsilon}^p}\mathbf{L})\sqrt{\frac{1}{2}}||\mathbf{n}_g||} \mathbf{n}_g \right]$$

$$= \left[ \mathbb{C}_e - \frac{\mathbb{C}_e : \mathbf{n}_f \otimes \mathbf{n}_g : \mathbb{C}_e}{\mathbf{n}_f : \mathbb{C}_e : \mathbf{n}_g + (\partial_{\mathbb{K}}f\partial_{\bar{\varepsilon}^p}\mathbb{K} + \partial_{\mathbf{L}}f\partial_{\bar{\varepsilon}^p}\mathbf{L})\sqrt{\frac{1}{2}}||\mathbf{n}_g||} \right] : \dot{\boldsymbol{\varepsilon}}, \tag{50}$$

with the elastic–plastic continuum tangent

$$\mathbb{C}_{ep} := \partial_{\boldsymbol{\varepsilon}}\boldsymbol{\sigma} = \left[ \mathbb{C}_e - \frac{\mathbb{C}_e : \mathbf{n}_f \otimes \mathbf{n}_g : \mathbb{C}_e}{\mathbf{n}_f : \mathbb{C}_e : \mathbf{n}_g + (\partial_{\mathbb{K}}f\partial_{\bar{\varepsilon}^p}\mathbb{K} + \partial_{\mathbf{L}}f\partial_{\bar{\varepsilon}^p}\mathbf{L})\sqrt{\frac{1}{2}}||\mathbf{n}_g||} \right]. \tag{51}$$

### 2.6. Integration algorithm

To obtain a numerical solution, the evolution equations of the internal variables $\boldsymbol{\varepsilon}^p$ and $\bar{\varepsilon}^p$ are discretized in time at Gauss-point level within a finite-element framework. For the time integration, the backward Euler integration scheme with a standard operator split (elastic predictor–plastic corrector) is used, following a proposal of Eidel (2005). Eidel (2005) introduced a time integration, which is based on the reduction to one scalar variable. The algorithmic treatment of the constitutive equations is shown in detail in the appendix. An in-deep description of integration schemes for elastic–plastic constitutive equations is given in Simo and Hughes (1998). The material model is implemented in Abaqus via the user interface UMAT (for Abaqus implicit) and VUMAT (for Abaqus explicit) (ABAQUS Manual, 2010).

## 3. Model verification and simulation results

In order to demonstrate the capabilities of the new material model, a complete yield surface parameter identification for the carbon epoxy IM7-8552 is presented in 3.1. Since not all required material tests are available, some reasonable assumptions are made for the missing material

**Table 1**
Determination of plastic potential parameters.

1. Give stress state (normalized)

$$\boldsymbol{\sigma}^{uni} = \begin{bmatrix} 0 & 0 & 0 \\ 0 & 1 & 0 \\ 0 & 0 & 0 \end{bmatrix} \left( \text{resp. } \boldsymbol{\sigma}^{s} = \begin{bmatrix} 0 & 1 & 0 \\ 1 & 0 & 0 \\ 0 & 0 & 0 \end{bmatrix}, \boldsymbol{\sigma}^{bi} = \begin{bmatrix} 0 & 0 & 0 \\ 0 & 1 & 0 \\ 0 & 0 & 1 \end{bmatrix}, \ldots \right)$$

2. Determination of $\nu^p$ and contractility $\kappa^p$
   Set initial values:  $\hat{Y}_U = 2\hat{Y}_S \rightarrow \varepsilon_{vol}^p = 0$, $\kappa^p = 0$, $\nu^p = 1$, $f_{uni}^{corr} = 1 \rightarrow \hat{Y}_U := 200$, $\hat{Y}_S = 100$
   (i) Give potential stresses:  $\hat{Y}_U := 200$, $\hat{Y}_S = 100$
   (ii) Calculate plastic strains, equivalent plastic strain and vol. plastic strain:

   $$\boldsymbol{\varepsilon}^{p,uni} = \mathbb{M} : \boldsymbol{\sigma}^{uni}$$

   $$\bar{\varepsilon}^p := \sqrt{\frac{1}{2}} \|\boldsymbol{\varepsilon}^p\| = \sqrt{\frac{1}{2} \varepsilon_{ij}^p \varepsilon_{ij}^p}$$

   $$\varepsilon_{vol}^p := \frac{1}{2} \operatorname{tr} \boldsymbol{\varepsilon}^p$$

   (iii) Calculate plastic Poisson ratio and plastic contractility:

   $$\nu_{23}^p := -\frac{\varepsilon_{22}^{p,uni}}{\varepsilon_{33}^{p,uni}}$$

   $$\kappa^p := -\frac{\varepsilon_{vol}^p}{\bar{\varepsilon}^p}$$

   Goto (i) and reduce $\hat{Y}_U$ until desired values of $\nu^p$ or $\kappa^p$ are achieved
3. Calculate correction factor $f_{uni}^{corr}$ (resp. $f_{bi}^{corr}, f_{s}^{corr}$)

   $$f_{uni}^{corr} := \frac{\varepsilon_{22}^{p,uni}}{\bar{\varepsilon}^p}$$
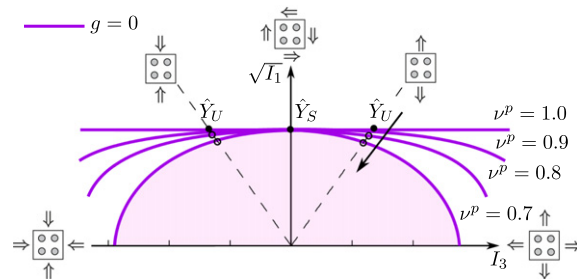


data. The objective in this section is to demonstrate the capabilities of the new material model. After deducing the material data for IM7-8552, simulations of the off-axis and transverse compression tests Koerber et al. (2010) presented in 3.2 and of the triaxial tests (Pae and Rhee, 1995) presented in 3.3 are shown as a model verification. It shall be demonstrated, that with just one parameter set both the off-axis compression tests and the triaxial tests can be simulated.

### 3.1. Yield surface of IM7-8552 carbon epoxy

The material model presented in this paper represents different hardening behavior in six stress states, as described in 2.4.1. However, a complete characterization of a composite is not always available. Especially when addressing biaxial and triaxial loadings the specimens are expensive to manufacture and the required test rigs are

complicated. A survey of test methods for composites under multiaxial and out-of-plane loading conditions is given in Olsson (2011). In addition, micromechanical models with a discrete representation of the constituents could provide relevant information to characterize the material under multiaxial stress states (González and LLorca, 2007; Totry et al., 2008). Hereafter, a characterization for the carbon epoxy IM7-8552 is derived, using experimental data from Koerber et al. (2010) and Pae and Rhee (1995). The deduction of missing material data and also possible test programs in order to conduct a complete material characterization for a unidirectional fiber matrix composite are discussed.

When modeling carbon fiber reinforced polymers (CFRP), the hardening behavior in the tensile range ($I_3 > 0$) is of minor importance. Just under combined shear-tension minor nonlinearities occur, whereas under uniaxial tension and biaxial tension primarily brittle

behavior is observed. This can be understood by considering yielding and fracture as concurring mechanisms. The greater the positive hydrostatic pressure, the more brittle the material behaves and fracture occurs before any significant yielding predominates. However, uniaxial and biaxial transverse tensile tests would complement the material characterization. Possible experimental rigs for biaxial tests are proposed by Welsh and Adams (2002), Welsh et al. (2006) and Smits et al. (2006). Off axis tensile tests are easy to perform and could serve as a validation. Since the simulation examples presented hereafter are in the compression range ($I_3 > 0$), the assumed non-linearities in the tensile range have no influence on these results. However, the uniaxial transverse tension and the biaxial transverse tension curves are assumed, based on computations using a representative volume element according (Melro, 2011) with a discrete representation of fibers and matrix.

In contrast to the uniaxial and biaxial transverse tensile behavior, the shear yielding behavior and the uniaxial and biaxial compression hardening behavior are essential to have a good constitutive representation for FRP. The transverse compression stress strain curve for IM7-8552 is directly measured in the 90° transverse compression tests (Koerber et al., 2010). The in-plane shear stress–strain curve is determined by a rotation of the stresses and strains measured in the 45° off-axis compression test into the shear plane, as described in Koerber et al. (2010). A transverse shear test for IM7-8552 does not exist. A test setup to perform transverse shear tests is presented in Pettersson and Neumeister (2006) and would complement the characterization of IM7-8552 presented in Koerber et al. (2010). An alternative to deduce the transverse shear behavior is the computation of representative volume elements modeling fiber and matrix (Melro, 2011, Ernst, 2009, Totry et al., 2008). Melro (2011) demonstrated that the in-plane shear yielding and the transverse shear yielding behavior are similar. This is plausible since both transverse shear and in-plane shear are matrix dominated loading states. Based on these observations, the transverse shear hardening curve is assumed by scaling down the in-plane shear yielding curve with a factor 0.95. Since the off-axis compression tests and triaxial tests are not sensitive to transverse shear, this assumption is not verified. A possible validation for the transverse shear behavior could be for instance laminate bending tests with a sufficient number of 90° layers in the middle.

Biaxial compression tests are not available for IM7-8552. Possible test setup for biaxial compression tests are suggested by Welsh and Adams (2002), Welsh et al. (2006) and Smits et al. (2006). In this paper, the biaxial compression hardening behavior is deduced using triaxial tests performed by Pae and Rhee (1995). Since the material tested by Pae and Rhee (1995) is a Scotchply SP-319 prepreg carbon epoxy, the behavior for IM7-8552 is deduced from these tests as explained in 3.3. Due to a lack of experimental data, the biaxial compression hardening curve for IM7-8552 is just assumed by scaling the uniaxial transverse compression hardening curve. This assumption is not experimentally verified. However, a scaling factor of 2.0 permits to approximate the triaxial tests (Pae and Rhee,

1995) presented in 3.3. The simulations of the triaxial tests have shown a strong sensitivity with respect to the biaxial transverse compression behavior, but not for simulating the off-axis compression tests. Hence it can be concluded, that the biaxial hardening behavior determines the plastic behavior in the presence of high pressure.

Having determined the material behavior in all required stress states, the hardening curves are obtained by reducing the total strains by the elastic part of the strains. For use in a finite element code, the hardening curves are required as true stresses vs. true plastic strains. A detailed description of preparing hardening curves out of experimental data can be found in Vogler (2011).

In Figs. 4 and 5 the previously derived hardening curves for carbon epoxy IM7-8552 are shown. In both illustrations, the left-hand side shows yield stress vs. corresponding plastic strains, the right-hand side shows stress vs. total strains. In Fig. 4 the in-plane and transverse shear hardening curves are given. Fig. 5 shows the hardening curves for uniaxial and biaxial compression and uniaxial and biaxial tension. The cross represents the respective failure point in each stress state. In both the uniaxial and biaxial tensile hardening curve it can be seen that there are just minor pre failure nonlinearities. This is exactly that range, where a ductile–brittle transition of the material behavior occurs, see also Fig. 6. Fig. 6 shows the representation of yield surface, failure surface and plastic potential in $I_3 - \sqrt{I_1}$ – invariant plane. The concentric lines illustrate the yield surface at different loading histories. They represent an inflation of the yield surface due to the applied isotropic hardening formulation. On the tensile side ($I_3 > 0$) the plastic behavior is just assumed in order to ensure the ductile–brittle transition observed in experiments. The failure surface "cuts" the yield surface. As soon as a certain stress state exceeds the failure surface, degradation
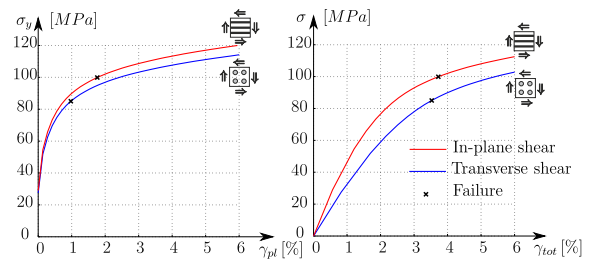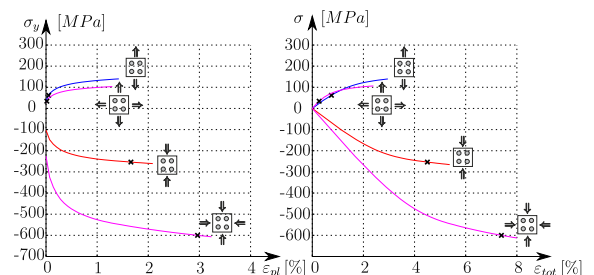


Fig. 4. Shear hardening behavior of IM7-8552.



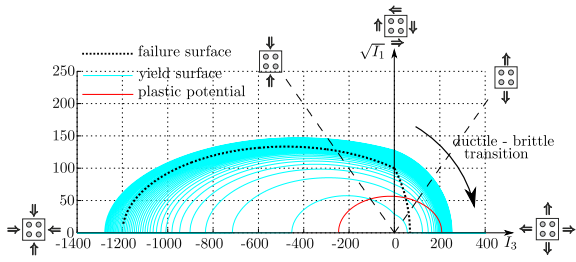Fig. 5. Uniaxial and biaxial hardening behavior of IM7-8552.

**Fig. 6.** Transversely-isotropic yieldsurface for IM7-8552 in $I_3 - \sqrt{I_1}$ invariant plane.
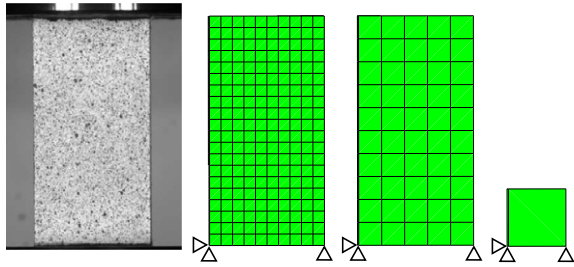


**Fig. 7.** Off-axis compression tests: Test specimen and FE-discretization.

starts controlled by the smeared crack model presented in Camanho et al. (2012).

### 3.2. Quasi-static off-axis compression tests

With the yield surface parameters derived in Section 3.1, the quasi-static off-axis and transverse compression tests of a Hex-Ply® IM7-8552 UD carbon epoxy presented in Koerber et al. (2010) are simulated. Since the in-plane shear behavior and the transverse compression behavior are directly obtained from the 45° respectively from the 90° test, the simulation of the off-axis tests is a verification of the proposed material model and identification procedure. According the test program Koerber et al. (2010), off-axis compression tests with fiber angles $\theta = 15°$, 30°, 45°, 60° and 75° and a transverse compression test ($\theta = 90°$) are simulated. To model the off axis tests, a single cubic element, a coarse mesh with 100 elements and a fine mesh with 800 elements are used, whereby the same boundary conditions as in the material tests are applied. That means, at the bottom the specimens are fixed whereas at the top (load application) the specimen can move in horizontal direction. In the experiments this is realized by a thin layer of Molybdenum–Disulfide ($MoS_2$) in order to minimize friction and to allow a lateral deflection. The test specimen used by Koerber et al. (2010) and the corresponding FE discretization showing the fine mesh, the coarse mesh and the single cubic element are depicted in Fig. 7. Abaqus (ABAQUS Manual, 2010) solid elements C3D8 are chosen for the discretization. The simulations are done with both Abaqus implicit (UMAT) and Abaqus explicit (VUMAT), where no noticeable difference
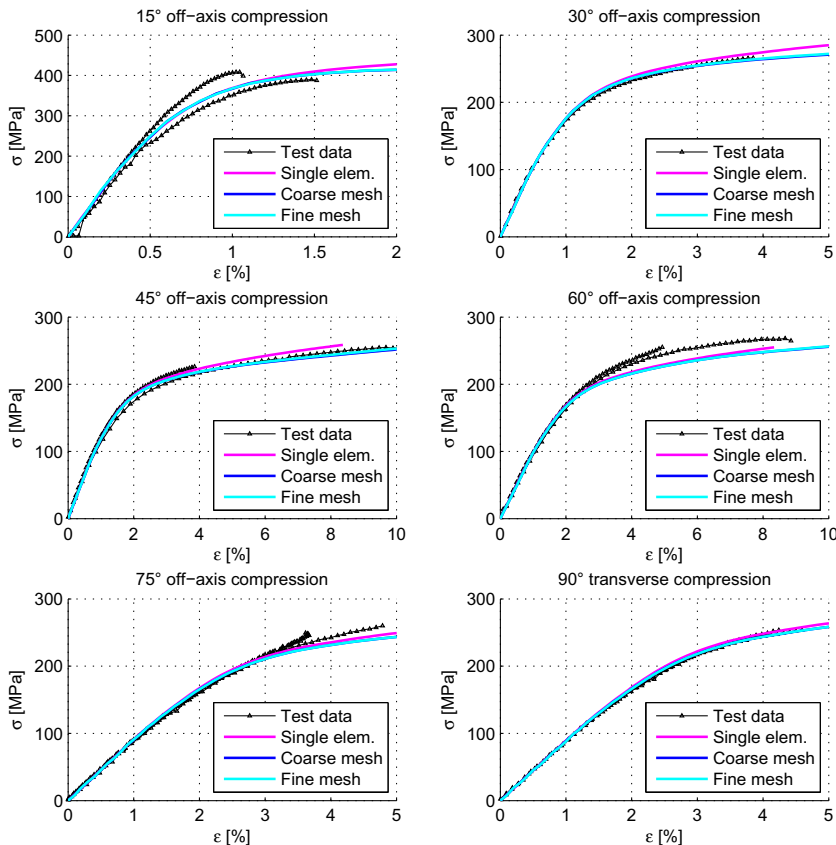


**Fig. 8.** Simulation of quasi-static off-axis and transverse compression tests for unidirectional carbon-epoxy IM7-8552.

between implicit and explicit analysis is observed. Fig. 8 shows the simulation results compared to the experimental data obtained by Koerber et al. (2010). In nearly all cases a very good agreement between the test data and the simulations can be seen. Just in the 60° off axis compression test, the hardening behavior is slightly underestimated. Furthermore, there is nearly no difference between the simulations with the coarse mesh, with the fine mesh and with the single cubic element.

### 3.3. Uniaxial compression tests under various hydrostatic pressures

Hereafter, the simulations of uniaxial compression tests of unidirectional 45° and 90° specimens under various levels of hydrostatic pressures are presented. The simulated tests shall reproduce the multiaxial stress states prevailing in the experiments performed by Pae and Rhee (1995). The testing system consists of two thick-walled pressure vessels for applying the hydrostatic pressure and a hydraulic cylinder for the subsequent uniaxial compression loading. For the test samples laminated square section blocks of dimension 0.953 mm × 0.953 mm × 3.81 mm are used. For a detailed description of the sample preparation and the experimental setup see (Pae and Rhee, 1995).

The material tested by Pae and Rhee is a Scotchply SP-319 prepreg system. For the simulations however, the material parameter identification for IM7-8552 carbon

epoxy presented in 3.1 is used. The objective is not to recover exactly the test results from Pae and Rhee (1995) with the material used there, but rather to show the applicability of the new model with respect to regard yielding in various stress states under multiaxial loading conditions. Hence, the simulations of the triaxial tests should be understood as a qualitative comparison in order to demonstrate the capabilities of the material model.

Since the experiments under high pressures were not performed with carbon epoxy IM7-8552, the behavior of this material is deduced from the experimental data measured by Pae and Rhee (1995) for the Scotchply SP-319 using a simple mapping procedure. Therefore, it is assumed that the qualitative behavior of both materials under high pressures is similar. That is, the measured curves under atmospheric pressure for the 45° off-axis test and for the 90° off-axis test of fiber epoxy IM7-8552 performed by Koerber et al. (2010) are scaled by a factor in order to assume a similar behavior as measured for the Scotchply SP-319 specimen by Pae and Rhee (1995). The same is done with the failure points for the 45° specimen and 90° specimen. This mapping procedure is illustrated in Fig. 9 for the 45° test sample. The lowest curve at atmospheric pressure is the curve measured in the 45° off-axis compression test by Koerber et al. (2010). The hardening curves and failure points at 1 kbar, 2 kbar and 3 kbar on the right hand side are just scaled in order to map the nonlinear material behavior measured for SP-319 at higher pressures to the
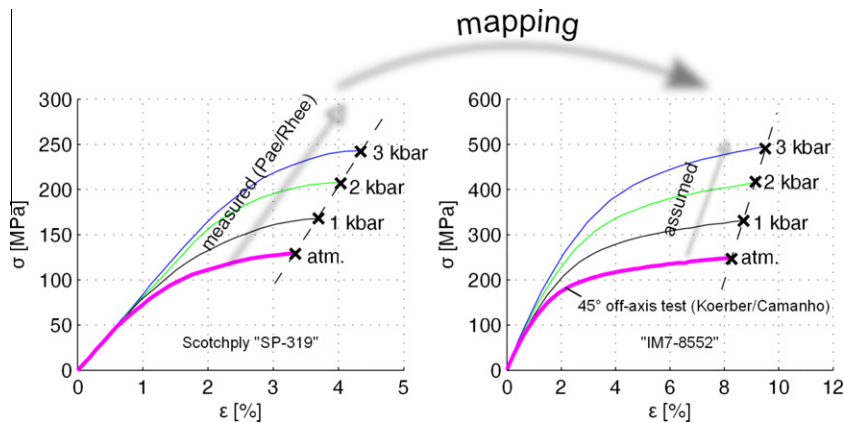


**Fig. 9.** Mapping procedure for the 45° test sample: measured curves from Pae and Rhee for Scotchply SP-319 (left) and assumed behavior for IM7-8552.
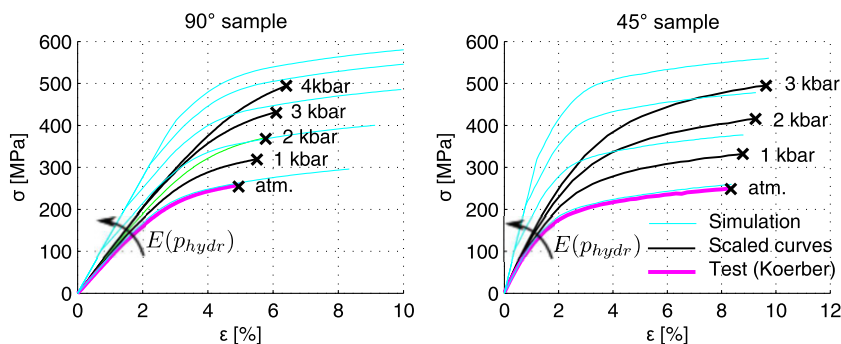


**Fig. 10.** Uniaxial compression tests under various levels of hydrostatic pressures, original elasticity parameters.
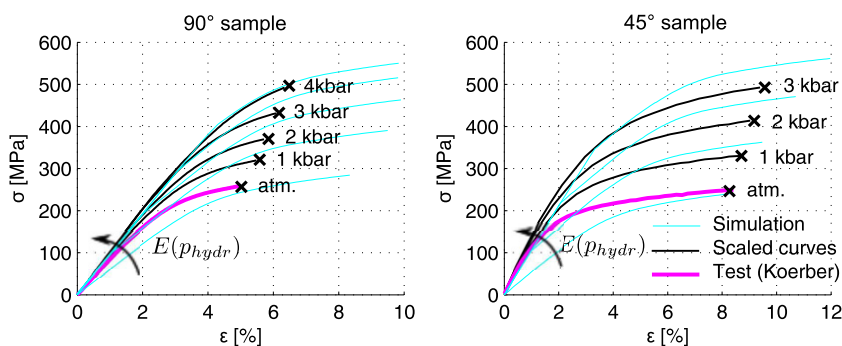
**Fig. 11.** Uniaxial compression tests under various levels of hydrostatic pressures, reduced elasticity parameters.

current material IM7-8552. Hence, the material curves and failure points on the right hand side at 1 kbar, 2 kbar and 3 kbar represent an assumed material behavior for IM7-8552 based on the experiments from Pae and Rhee (1995).

The Finite Element model is discretized with C3D8 solid elements. A coarse mesh with $1 \times 1 \times 4$ elements and a fine mesh with $4 \times 4 \times 16$ elements are used. As before, simulations are done both in Abaqus implicit and Abaqus explicit. According to the tests, the simulations are done in two steps. In a first load step, the corresponding hydrostatic pressure is applied, followed by a second load step, where the uniaxial compression is applied. At first, the elastic properties are left unchanged for all levels of hydrostatic pressures. These are the elastic properties measured under atmospheric pressure. The results for the 45° and for the 90° specimen with the original elasticity parameters are shown in Fig. 10. It is observed that for lower pressures the curves show a good correlation with the assumed curves via scaling. The higher the applied pressure, the more the simulated curves differ from the assumed curves. The reason for this effect is that not only the plastic behavior of the epoxy resin changes due to high hydrostatic pressure, but also the elastic properties. This has been also observed by Dupaix and Boyce (2007) and Mi and Zheng (1998). In order to demonstrate this effect, the elastic properties are reduced in a second simulation, see Fig. 11. The elasticity parameters are now chosen in order to fit the curve for the highest level of hydrostatic pressures in each case, i.e. 3 kbar resp. 4 kbar for the 90° test sample, whereby the plastic parameters are left unchanged. The results in Fig. 11 show a good agreement with the curves under higher pressures (3 kbar and 4 kbar) but the curves at atmospheric pressure and lower hydrostatical pressures do not coincide very well. Summarizing the results it can be concluded that by controlling yielding behavior in biaxial compression the nonlinear behavior under high pressures can be captured approximately. However, the change of the elastic parameters should also be taken into account. This can be accomplished with the introduction of an evolution equation that describes the phase transformation of the epoxy resin due to a drop of the glass transition temperature in the presence of high hydrostatic pressures.

## 4. Conclusions and outlook

The new material model presented in this paper is able to predict the plastic deformation of polymer composite mate-

rials under general stress states using a simple model identification procedure based on stress-plastic strain curves. In addition, the new non-associative flow rule enables the correct prediction of the plastic Poisson's ratio. The comparison between the model predictions and experimental data obtained in off-axis compression test specimens showed an excellent agreement. The simulations of uniaxial compression tests under various levels of hydrostatic pressure show a good approximation of the pressure dependent yielding behavior by simply assuming a biaxial compression hardening curve. However, the reduction of the elastic properties due to hydrostatic pressure has to be taken into account in future developments. A visco-plastic extension of the model can be done easily from a numerical point of view. However, in order to capture the expected highly non-linear rate dependency (Koerber et al., 2010), further characterization tests for at least 2 higher strain rate regimes have to be performed. Furthermore off-axis tensile tests and transverse shear tests of IM7-8552 would complement the proposed material characterization. Taking into account that the material model controls yielding behavior in the tensile range ($I_3 > 0$), this constitutive model is also suitable for organic sheets and glass fiber reinforced fabrics (GFRP), where more pronounced nonlinearities under tension are observed. In future investigations, the model has to be validated at laminate level. Therefore, laminate bending tests, component tests, open and filled hole tests and bolted joints should be simulated. The combination of the plasticity model presented here with a smeared crack model that predicts the onset and propagation of the ply failure mechanisms is presented in an accompanying paper.

## Acknowledgement

## Appendix A. Backward Euler time integration, following a proposal of Eidel (2005)

Applying the backward Euler algorithm in the time interval $\Delta t_{n+1} = t_{n+1} - t_n$ with $\Delta \gamma_{n+1} = \Delta t_{n+1} \gamma$ leads to the update formula of the plastic strains at $t_{n+1}$:

$$\boldsymbol{\varepsilon}_{n+1}^p = \boldsymbol{\varepsilon}_n^p + \Delta t \dot{\boldsymbol{\varepsilon}}_{n+1}^p = \boldsymbol{\varepsilon}_n^p + \Delta\gamma \partial_{\boldsymbol{\sigma}} g_{n+1}. \tag{52}$$

The assumed additive split of the strains Eq. (1) and the elastic law give the elastic trial step:

$$\boldsymbol{\varepsilon}_{n+1}^{tr} := \boldsymbol{\varepsilon}_{n+1} - \boldsymbol{\varepsilon}_n^p = \mathbb{C}_e^{-1}\boldsymbol{\sigma}_{n+1} + \Delta\gamma_{n+1}\partial_{\boldsymbol{\sigma}} g_{n+1}, \\ \boldsymbol{\sigma}_{n+1}^{tr} := \mathbb{C}_e : \boldsymbol{\varepsilon}_{n+1}^{tr} = \boldsymbol{\sigma}_{n+1} + \Delta\gamma_{n+1}\mathbb{C}_e : \partial_{\boldsymbol{\sigma}} g_{n+1}. \tag{53}$$

Using Eq. (20), the elastic trial stresses read:

$$\boldsymbol{\sigma}_{n+1}^{tr} = \boldsymbol{\sigma}_{n+1} + \Delta\gamma_{n+1}\mathbb{C}_e : \mathbb{M} : \boldsymbol{\sigma}_{n+1} \\ = \left(\mathbb{I} + \Delta\gamma_{n+1}\mathbb{C}_e : \mathbb{M}\right) : \boldsymbol{\sigma}_{n+1}. \tag{54}$$

Conversion to $\boldsymbol{\sigma}_{n+1}$ yields:

$$\boldsymbol{\sigma}_{n+1} = \left(\mathbb{I} + \Delta\gamma_{n+1}\mathbb{C}_e : \mathbb{M}\right)^{-1} : \boldsymbol{\sigma}_{n+1}^{tr} \\ = \mathbb{F}_{n+1} : \boldsymbol{\sigma}_{n+1}^{tr}, \tag{55}$$

with $\mathbb{F}_{n+1} = \left(\mathbb{I} + \Delta\gamma_{n+1}\mathbb{C}_e : \mathbb{M}\right)^{-1}$.

In case of plastic yielding, $f_{n+1}(\boldsymbol{\sigma}_{n+1}^{tr}, \mathbf{A}, \bar{\varepsilon}_{n+1}^p) \geqslant 0$ holds, and the yield condition gives an algebraic constraint that has to be fulfilled at the end of the considered time step $t_{n+1}$:

$$f_{n+1}(\boldsymbol{\sigma}_{n+1}, \mathbf{A}, \bar{\varepsilon}_{n+1}^p) \overset{!}{=} 0. \tag{56}$$

Inserting Eq. (55) into the yield function Eq. (56), gives an equation to determine the consistency parameter $\Delta\gamma_{n+1}$, which is solved with the Newton–Raphson method. In a non-iterated step, the residual reads:

$$R^f|_{n+1}^{(k)} := f_{n+1}^{(k)} = \frac{1}{2}\boldsymbol{\sigma}_{n+1}^{(k)} : \mathbb{K}^{(k)} : \boldsymbol{\sigma}_{n+1}^{(k)} + \mathbf{L}^{(k)} \\ : \boldsymbol{\sigma}_{n+1}^{(k)} - 1 \overset{!}{=} 0, \tag{57}$$

where iterations are counted with index $(k)$. The residual $R_{n+1}^f := f_{n+1}$ is developed into a Taylor-series at $t_{n+1}$ and linearized:

$$R^f|_{n+1}^{(k)} := f(\boldsymbol{\sigma}_{n+1}^{(k)}(\Delta\gamma_{n+1}^{(k)})) \\ \mathrm{Lin}\left[R^f|_{n+1}^{(k)}\right] = f_{n+1}^{(k)} + \Delta^2\gamma_{n+1}^{(k)}\frac{\partial f_{n+1}^{(k)}}{\partial\Delta\gamma_{n+1}^{(k)}} \overset{!}{=} 0. \tag{58}$$

Eq. (58) can be solved for the increment of the consistency parameter $\Delta\gamma_{n+1}^{(k)}$. Therefore, the root of the linearized residual in Eq. (58) is needed:

$$\Delta^2\gamma_{n+1}^{(k)} = -\frac{f|_{n+1}^{(k)}}{\frac{\partial f|_{n+1}^{(k)}}{\partial\gamma_{n+1}^{(k)}}}. \tag{59}$$

The update of the consistency parameter reads:

$$\Delta\gamma_{n+1}^{(k+1)} = \Delta\gamma_{n+1}^{(k)} + \Delta^2\gamma_{n+1}^{(k)}. \tag{60}$$

The required derivative $\partial_{\Delta\gamma}f_{n+1}^{(k)}$ in Eqs. (58) and (59) and the complete formula of the updated consistency parameter $\Delta\gamma_{n+1}^{(k+1)}$ (60) is derived hereafter.

The algorithmic consistent elastic–plastic material tangent reads:

$$\mathbb{C}_{ep}^{algo} = \mathbb{F}_{n+1} : \left(\mathbb{C}_e - \frac{\mathbb{C}_e : \mathbb{M} : \boldsymbol{\sigma}_{n+1} \otimes (\mathbb{K}_{n+1} : \boldsymbol{\sigma}_{n+1} + \mathbf{L}_{n+1}) : \mathbb{F}_{n+1} : \mathbb{C}_e}{(\mathbb{K}_{n+1} : \boldsymbol{\sigma}_{n+1} + \mathbf{L}_{n+1}) : \mathbb{F}_{n+1} : \mathbb{C}_e : \mathbb{M} : \boldsymbol{\sigma}_{n+1} + \frac{\partial f_{n+1}}{\partial\gamma_{n+1}}}\right), \tag{61}$$

with the derivative $\frac{\partial f_{n+1}}{\partial\Delta\gamma_{n+1}}$ given in Eq. (62).

The complete integration algorithm is summarized in Table 2. A scheme of the Euler backward integration algorithm is shown in Fig. 12.

**Derivative $\partial_{\Delta\gamma}f_{n+1}^{(k)}$:**

Hereafter, the derivative $\partial_{\Delta\gamma}f_{n+1}^{(k)}$ needed in Eqs. (58) and (59) is derived. For reasons of readability the indices $(n+1)$ and $(k)$ are omitted. Applying the chain rule, yields:

$$\frac{\partial f}{\partial\Delta\gamma} = \frac{\partial f}{\partial\boldsymbol{\sigma}} : \frac{\partial\boldsymbol{\sigma}}{\partial\Delta\gamma} + \frac{\partial f}{\partial\mathbb{K}}\cdots\frac{\partial\mathbb{K}}{\partial\Delta\gamma} + \frac{\partial f}{\partial\mathbf{L}} : \frac{\partial\mathbf{L}}{\partial\Delta\gamma}, \tag{62}$$

with the partial derivatives $\partial_{\mathbb{K}}f$ and $\partial_{\mathbf{L}}f$:

$$\frac{\partial f}{\partial\mathbb{K}} = \boldsymbol{\sigma}\otimes\boldsymbol{\sigma}, \\ \frac{\partial f}{\partial\mathbf{L}} = \mathbf{L}\otimes\mathbf{1}. \tag{63}$$

The partial derivative $\partial_{\boldsymbol{\sigma}}f$ is known from Eq. (15), the partial derivative $\partial_{\Delta\gamma}\boldsymbol{\sigma}$ can be determined applying the chain rule and using the condition $\partial_{\Delta\gamma}\boldsymbol{\sigma}^{tr} \overset{!}{=} \mathbf{0}$ :

**Table 2**
General-return algorithm.

---

1. Input data at Gauss point level

   total deformation at $t_{n+1} : \boldsymbol{\varepsilon}_{n+1}$
   internal variables at $t_n : \boldsymbol{\varepsilon}_n^p, \bar{\varepsilon}^p$

2. 1st operator: elastic predictor

   $\boldsymbol{\varepsilon}_{n+1}^{tr} = \boldsymbol{\varepsilon}_{n+1} - \boldsymbol{\varepsilon}_n^p$
   $\sigma_{n+1}^{tr} = \mathbb{C}_e : \boldsymbol{\varepsilon}_{n+1}^{tr}$

3. 2nd operator: plastic corrector
   Local Newton Iteration
   $k = 0$ Set initial values $\boldsymbol{\sigma}_{n+1}^{(k=0)} = \boldsymbol{\sigma}_{n+1}^{tr}$, $(\bar{\varepsilon}_{n+1}^p)^{(k=0)} = \bar{\varepsilon}_n^p$, $\Delta\gamma_{n+1}^{(k=0)} = 0$

   (i)  $\mathbb{F}_{n+1}^{(k)} = \left[\mathbb{I} + \Delta\gamma_{n+1}^{(k)}\mathbb{C}_e : \mathbb{M}\right]^{(-1)}$

   $\boldsymbol{\sigma}_{n+1}^{(k)} = \mathbb{F}_{n+1}^{(k)} : \boldsymbol{\sigma}_{n+1}^{tr}$

   (ii) Table Lookup:

   $\bar{\varepsilon}^p \to$ Hardening Curves $\to \alpha_1^{(k)}, \alpha_2^{(k)}, \alpha_3^{(k)}, \alpha_{32}^{(k)}$
   $\to \mathbb{K}_{n+1}^{(k)}, \mathbf{L}_{n+1}^{(k)}$
   $f_{n+1}^{(k)} = \frac{1}{2}\boldsymbol{\sigma}_{n+1}^{(k)} : \mathbb{K}_{n+1}^{(k)} : \boldsymbol{\sigma}_{n+1}^{(k)} + \mathbf{L}_{n+1}^{(k)} : \boldsymbol{\sigma}_{n+1}^{(k)} - 1$
   if $f_{n+1}^{(k)} \leqslant$ *TOL* Goto 4., else continue

   (iii)  $\Delta^2\gamma_{n+1}^{(k)} = -\frac{f|_{n+1}^{(k)}}{\frac{\partial f|_{n+1}^{(k)}}{\partial\gamma_{n+1}^{(k)}}}$

   (iv)  $\Delta\gamma_{n+1}^{(k+1)} = \Delta\gamma_{n+1}^{(k)} + \Delta^2\gamma_{n+1}^{(k)}$

   $(\bar{\varepsilon}_{n+1}^p)^{(k+1)} = (\bar{\varepsilon}_{n+1}^p)^{(k)} + \Delta^2\gamma_{n+1}^{(k)}||\mathbb{M} : \boldsymbol{\sigma}_{n+1}^{(k)}||$

   (v) $k \leftarrow k + 1$

4. Update internal variables at $t_{n+1}$

   $\boldsymbol{\sigma}_{n+1} = \boldsymbol{\sigma}_{n+1}^{(k)}, \Delta\gamma_{n+1} = \Delta\gamma_{n+1}^k, \bar{\varepsilon}_{n+1}^p = (\bar{\varepsilon}_{n+1}^p)^k$
   $\boldsymbol{\varepsilon}_{n+1}^p = \boldsymbol{\varepsilon}_n^p + \Delta\gamma_{n+1}[\mathbb{M} : \boldsymbol{\sigma}_{n+1}]$

5. Algorithmic tangent modulus

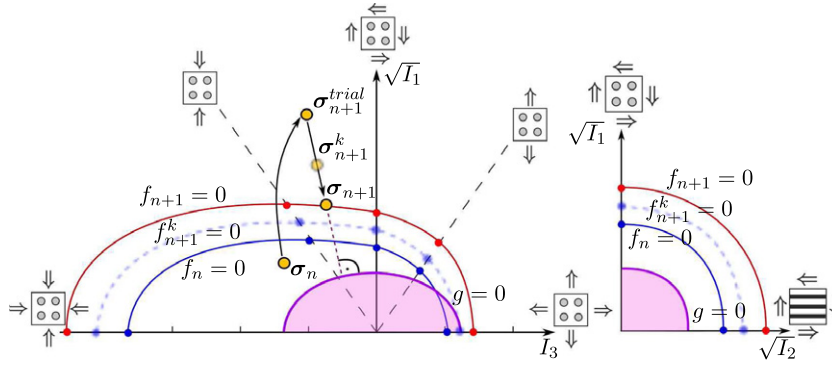   $\mathbb{C}_{ep}^{algo} = \frac{d\boldsymbol{\sigma}_{n+1}}{d\boldsymbol{\varepsilon}_{n+1}}$

---

**Fig. 12.** Scheme of Euler backward return algorithm.

$$0 = \partial_{\Delta\gamma}[(\mathbb{I} + \Delta\gamma\mathbb{C}_e : \mathbb{M}) : \boldsymbol{\sigma}] = \partial_{\Delta\gamma}[\mathbb{F}^{-1} : \boldsymbol{\sigma}] = (\partial_{\Delta\gamma}\mathbb{F}^{-1})$$
$$: \boldsymbol{\sigma} + \mathbb{F}^{-1} : \partial_{\Delta\gamma}\boldsymbol{\sigma}. \tag{64}$$

Conversion yields:

$$\partial_{\Delta\gamma}\boldsymbol{\sigma} = -\mathbb{F} : \partial_{\Delta\gamma}\mathbb{F}^{-1} : \boldsymbol{\sigma} = -\mathbb{F} : \mathbb{C}_e : \mathbb{M} : \boldsymbol{\sigma}. \tag{65}$$

The derivative $\partial_{\Delta\gamma}\mathbb{K}$ reads:

$$\frac{\partial\mathbb{K}}{\partial\Delta\gamma} = \frac{\partial\mathbb{K}}{\partial\bar{\varepsilon}^p}\frac{\partial\bar{\varepsilon}^p}{\partial\Delta\gamma}, \tag{66}$$

with

$$\frac{\partial\mathbb{K}}{\partial\bar{\varepsilon}^p} = \frac{\partial\mathbb{K}}{\partial\alpha_1}\frac{\partial\alpha_1}{\partial\bar{\varepsilon}^p} + \frac{\partial\mathbb{K}}{\partial\alpha_2}\frac{\partial\alpha_2}{\partial\bar{\varepsilon}^p} + \frac{\partial\mathbb{K}}{\partial\alpha_{32}}\frac{\partial\alpha_{32}}{\partial\bar{\varepsilon}^p}$$
$$= (\mathbb{P}^{pind} - \mathbb{P}_\mathbf{A}^{pind})\frac{\partial\alpha_1}{\partial\bar{\varepsilon}^p} + \mathbb{P}_\mathbf{A}^{pind}\frac{\partial\alpha_2}{\partial\bar{\varepsilon}^p} + 2(\mathbf{1} - \mathbf{A}) \otimes (\mathbf{1}$$
$$- \mathbf{A})\frac{\partial\alpha_{32}}{\partial\bar{\varepsilon}^p}, \tag{67}$$

and the derivative $\partial_{\Delta\gamma}\mathbf{L}$ reads

$$\frac{\partial\mathbf{L}}{\partial\Delta\gamma} = \frac{\partial\mathbf{L}}{\partial\bar{\varepsilon}^p}\frac{\partial\bar{\varepsilon}^p}{\partial\Delta\gamma}, \tag{68}$$

with

$$\frac{\partial\mathbf{L}}{\partial\bar{\varepsilon}^p} = \frac{\partial\mathbf{L}}{\partial\alpha_3}\frac{\partial\alpha_3}{\partial\bar{\varepsilon}^p}\frac{\partial\bar{\varepsilon}^p}{\partial\Delta\gamma} = (\mathbf{1} - \mathbf{A})\frac{\partial\alpha_3}{\partial\bar{\varepsilon}^p}\frac{\partial\bar{\varepsilon}^p}{\partial\Delta\gamma}. \tag{69}$$

The derivation $\frac{\partial\bar{\varepsilon}^p}{\partial\Delta\gamma}$ in Eq. (66) and Eq. (68) yields:

$$\frac{\partial\bar{\varepsilon}^p}{\partial\Delta\gamma} = \sqrt{\frac{1}{2}}||\mathbb{M} : \boldsymbol{\sigma}|| + \Delta\gamma\sqrt{\frac{1}{2}}\frac{\partial||\mathbb{M} : \boldsymbol{\sigma}||}{\partial\boldsymbol{\sigma}}\frac{\partial\boldsymbol{\sigma}}{\partial\Delta\gamma} = \sqrt{\frac{1}{2}}||\mathbb{M}$$
$$: \boldsymbol{\sigma}|| + \Delta\gamma\sqrt{\frac{1}{2}}\mathbb{M}\frac{\boldsymbol{\sigma}}{||\boldsymbol{\sigma}||}\frac{\partial\boldsymbol{\sigma}}{\partial\Delta\gamma}, \tag{70}$$

with the derivative $\frac{\partial\boldsymbol{\sigma}}{\partial\Delta\gamma}$ given in Eq. (65).

Furthermore, the following derivatives of the yield surface parameters with respect to the equivalent plastic strain are required:

$$\frac{\partial\alpha_1}{\partial\bar{\varepsilon}_{n+1}^p}, \quad \frac{\partial\alpha_2}{\partial\bar{\varepsilon}_{n+1}^p}, \quad \frac{\partial\alpha_3}{\partial\bar{\varepsilon}_{n+1}^p} \quad \text{and} \quad \frac{\partial\alpha_{32}}{\partial\bar{\varepsilon}_{n+1}^p}. \tag{71}$$

These derivatives can be obtained easily from Eqs. (24), (25), (28), (29), (32) and (33). Doing these trivial derivations, the derivatives of the corresponding yield stress with respect to $\bar{\varepsilon}^p$ are needed. Therefore, in each iteration step

($k$) both the yield stress and the slope of the hardening curves (i.e. the current hardening modulus of each loading state) are updated. In the material routine, this is done with a so called Table lookup. That is, the hardening data can be input as tabulated data giving yield stress vs. corresponding plastic strain in the input file. Hereby, the equivalent plastic strain $(\bar{\varepsilon}^p)_{n+1}^{(k)}$ of each iteration step serves as input value for reading in the yield stress and the corresponding hardening modulus of each prescribed loading state. The Table lookup is schematically depicted in the small figures in Section 2.4.1, the realization in the material routine is schematically shown in Fig. 12. Since the hardening curves are given as yield stress vs. corresponding plastic strain, relation Eq. (23) is used to obtain the correct plastic strain $\varepsilon_{uni}^p$, $\varepsilon_{bi}^p$ and $\varepsilon_s^p$ for each hardening curve. With Eq. (63) to Eq. (71), all derivatives are known and the root of the linearized residual Eq. (58) reads:

**Table 3**
Conversion of elasticity constants for transverse isotropy.

- Symmetry of elasticity tensor:
  $\frac{v_{12}}{E_{22}} = \frac{v_{21}}{E_{11}}$; $\quad \frac{v_{13}}{E_{33}} = \frac{v_{31}}{E_{11}}$; $\quad \frac{v_{23}}{E_{33}} = \frac{v_{32}}{E_{22}}$

- Coefficients of invariant representation:

  $\lambda = E_{22}(v_{23} + v_{31}v_{13})/D$
  $\alpha = E_{22}[v_{31}(1 + v_{32} - v_{13}) - v_{32}]/D$
  $\beta = E_{11}(1 - v_{32}v_{23})/D - E_{22}[1 - v_{21}(v_{12} + 2(1 + v_{23})]/D - 4\mu_{12}$
  $\mu_l = \mu_{12}$
  $\mu_t = \mu_{23}$
  $D = 1 - v_{32}^2 - 2v_{13}v_{31} - 2v_{32}v_{31}v_{13}$

- Engineering constants:
  $E_{22} = E_{33}, \quad v_{23} = v_{32}, \quad v_{12} = v_{13}, \quad v_{21} = v_{31}, \quad \mu_{12} = \mu_{13}$

  $E_{11} = -(\lambda\mu_t - 4\lambda\mu_l - \lambda\beta + 2\mu_t^2 - \beta\mu_t - 2\alpha\mu_t - 4\mu_l\mu_t + \alpha^2)/$
  $\quad (\lambda + \mu_t)$
  $E_{22} = -4\mu_t(\lambda\mu_t - 4\mu_l\lambda - \beta\lambda + 2\mu_t^2 - \beta\mu_t - 2\alpha\mu_t$
  $\quad - 4\mu_t\mu_l + \alpha^2)/D_t$
  $v_{12} = 2\mu_t(\lambda + \alpha)/D_t$
  $v_{21} = (\lambda + \alpha)/(2\lambda + 2\mu_t)$
  $v_{23} = -(\alpha^2 + 2\lambda\mu_t - \beta\lambda - 4\mu_l\lambda)/D_t$
  $\mu_{12} = \mu_l$
  $\mu_{23} = \mu_t$
  $D_t = 4\mu_l\lambda + \beta\lambda - 4\mu_t^2 + 4\mu_t\alpha + 2\beta\mu_t + 8\mu_l\mu_t - \alpha^2$

$$\Delta^2 \gamma_{n+1}^{(k)} = -\frac{f|_{n+1}^{(k)}}{\frac{\partial f|_{n+1}^{(k)}}{\partial \Delta \gamma_{n+1}^{(k)}}} = \frac{f|_{n+1}^{(k)}}{\left[\left(\mathbb{K}_{n+1}^{(k)} : \boldsymbol{\sigma}_{n+1}^{(k)} + \mathbf{L}_{n+1}^{(k)}\right) : \mathbb{F}_{n+1}^{(k)} : \mathbb{C}_e : \mathbb{M} : \boldsymbol{\sigma}_{n+1}^{(k)} + \boldsymbol{\sigma}_{n+1}^{(k)} \otimes \boldsymbol{\sigma}_{n+1}^{(k)} \cdots \frac{\partial \mathbb{K}_{n+1}^{(k)}}{\partial \Delta \gamma_{n+1}^{(k)}} + \mathbf{L}_{n+1}^{(k)} \otimes \mathbf{1} : \frac{\partial \mathbf{L}_{n+1}^{(k)}}{\partial \Delta \gamma_{n+1}^{(k)}}\right]} . \tag{72}$$

## References

ABAQUS Documentation (v6.10) [Computer software manual], 2010.
Boehler, J. (Ed.), 1987. Applications of Tensor Functions in Solid Mechanics. Springer.
Camanho, P., Bessa, M., Catalanotti, G., Vogler, M., Rolfes, R., 2012. Modeling the inelastic deformation and fracture of polymer composites – Part II: Smeared crack model. Mechanics of Materials.
Chang, F.K., Chang, K.-Y., 1987. A progressive damage model for laminated composites containing stress concentrations. Journal of Composite Materials 21 (9), 834–855, http://dx.doi.org/10.1016/j.mechmat.2012.12.001.
Dupaix, R.B., Boyce, M.C., 2007. Constitutive modeling of the finite strain behavior of amorphous polymers in and above the glass transition. Mechanics of Materials 39 (1), 39–52.
Eidel, B., 2005. Anisotropic Inelasticity – Modelling, Simulation, Validation. Shaker Verlag (Doctoral dissertation, Fachbereich Bauingenieurwesen und Geodäsie, Technische Universität Darmstadt).
Ernst, G., 2009. Multiscale analysis of textile composites – stiffness and strength. Doctoral dissertation, Leibniz Universität Hannover. (Mitteilungen des Instituts für Statik und Dynamik der Leibniz Universität Hannover 10/2009).
González, C., LLorca, J., 2007. Mechanical behavior of unidirectional fiber reinforced polymers under transverse compression: microscopic mechanisms and modeling. Composites Science and Technology 67 (13), 2795–2806.
Koerber, H., Xavier, J., Camanho, P., 2010. High strain rate characterisation of unidirectional carbon-epoxy IM7-8552 in transverse compression and in-plane shear using digital image correlation. Mechanics of Materials 42 (11), 1004–1019.
Maimi, P., Camanho, P., Mayugo, J., Turon, A., 2011. Matrix cracking and delamination in laminated composites. Part I: Ply constitutive law, first ply failure and onset of delamination. Mechanics of Materials 43 (4), 169–185.
Melro, A.R., 2011. Analytical and numerical modelling of damage and fracture of advanced composites. Unpublished doctoral dissertation, Faculdade de Engenharia da Universidade do Porto.
Mi, Y., Zheng, S., 1998. A new study of glass transition of polymers by high pressure DSC. Polymer 39 (16), 3709–3712.
Olsson, R., 2011. A survey of test methods for multiaxial and out-of-plane strength of composite laminates. Composites Science and Technology 71 (6), 773–783.
Pae, K., Rhee, K., 1995. Effects of hydrostatic pressure on the compressive behavior of thick laminated 45 and 90 unidirectional graphite fiber/epoxy-matrix composites. Composites Science and Technology 53 (3), 281–287.

Pettersson, K.B., Neumeister, J.M., 2006. A tensile setup for the IDNS composite shear test. Composites Part A: Applied Science and Manufacturing 37 (2), 229–242.
Pinho, S., Iannucci, L., Robinson, P., 2006. Physically based failure models and criteria for laminated fibre-reinforced composites with emphasis on fibre kinking. Part II: FE implementation. Composites Part A: Applied Science and Manufacturing 37 (5), 766–777.
Rogers, T., 1987. Yield criteria, flow rules and hardening in anisotropic plasticity. In: Boehler, J. (Ed.), Yielding, Damage and Failure of Anisotropic Solids, vol. 5. EGF Publication, pp. 53–79.
Rolfes, R., Ernst, G., Vogler, M., Hühne, C., 2008. Material and failure models for textile composites. In: Camanho, P.P., D/'avila, C.G., Pinho, S.T., Remmers, J. (Eds.), Mechanical Response of Composites, vol. 10. Springer (p. in print).
Schröder, J., 1995. Theoretische und algorithmische Konzepte zur phäanomenologischen Beschreibung anisotropen Materialverhaltens. Doctoral dissertation, Universität Hannover.
Simo, J., Hughes, T., 1998. Computational Inelasticity. Springer, New York.
Smits, A., Hemelrijck, D.V., Philippidis, T., Cardon, A., 2006. Design of a cruciform specimen for biaxial testing of fibre reinforced composite laminates. Composites Science and Technology 66 (7–8), 964–975.
Spencer, A., 1972. Deformations of Fibre-Reinforced Materials. Clarendon Press, Oxford.
Spencer, A., 1987. Kinematic constraints, constitutive equations and failure rules for anisotropic materials. In: Boehler, J. (Ed.), Applications of Tensor Functions in Solid Mechanics. Springer, pp. 187–201.
Sun, C.T., Chen, J.L., 1989. A simple flow rule for characterizing nonlinear behavior of fiber composites. Journal of Composite Materials 23, 1009–1020.
Totry, E., González, C., LLorca, J., 2008. Failure locus of fiber-reinforced composites under transverse compression and out-of-plane shear. Composites Science and Technology 68 (3–4), 829–839.
Vogler, M., 2011. Viskoplastische Stoffgesetze für Thermoplaste in LSDYNA: Theorie und Aspekte der Programmierung. VDM Verlag, New York.
Vogler, M., Ernst, G., Rolfes, R., 2010. Invariant based transversely isotropic material and failure model for fiber-reinforced polymers. Computers, Materials & Continua 16 (1), 25–49.
Welsh, J.S., Adams, D.F., 2002. An experimental investigation of the biaxial strength of IM6/3501-6 carbon/epoxy cross-ply laminates using cruciform specimens. Composites Part A: Applied Science and Manufacturing 33 (6), 829–839.
Welsh, J.S., Mayes, J.S., Biskner, A.C., 2006. 2-D biaxial testing and 33 failure predictions of IM7/977-2 carbon/epoxy quasi-isotropic laminates. Composite Structures 75 (1–4), 60–66.